# Nanoscale

Accepted Manuscript


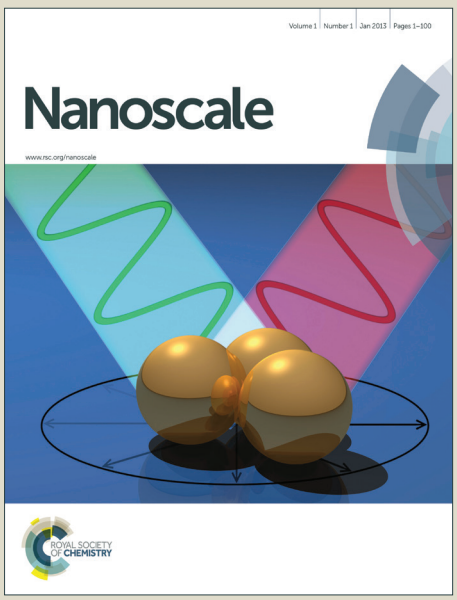





ROYAL SOCIETY OF CHEMISTRY

www.rsc.org/nanoscale

Journal Name

RSCPublishing

ARTICLE

# Large-scale growth of hierarchical transition-metal vanadate nanosheets on metal meshes as monolith catalysts for De-$NO_x$ reaction

Cite this: DOI: 10.1039/x0xx00000x

Received 00th January 2012,
Accepted 00th January 2012

DOI: 10.1039/x0xx00000x

www.rsc.org/

Lei Huang, [a] Xin Zhao, [a] Lei Zhang, [b] Liyi Shi, [a] Jianping Zhang [a] and Dengsong Zhang* [a]

A facile method is developed for the large-scale growth of hierarchical transition-metal (Cu, Fe, and Ni) vanadate nanosheets on corresponding metal mesh as supports. The hierarchical transition-metal vanadate nanosheets were *in-situ* grown on the metal meshes through an orientational etching process and simultaneous nucleation and growth process. Interestingly, the morphologies of the vanadate nanosheets are governed by the balance between dissolution rate and nucleation rate. Thus, the sizes and the thicknesses of the nanosheets could be facilely controlled by the reaction duration, the acidity of the solution and the concentration of vanadate precursor. Furthermore, the hierarchical transition-metal vanadate nanosheets supported on metal meshes are used as monolith catalysts for the selective catalytic reduction (SCR) of NO with $NH_3$. The iron mesh based monolith catalyst shows excellent de-$NO_x$ performances with high efficiency and stability in the presence of $SO_2$ and $H_2O$, which provide a promising monolith de-$NO_x$ catalyst for stationary source at medium temperatures.

## 1. Introduction

Hierarchical nanostructures have been attracting sustained attention in the applications of catalysis,[1-3] solar cells,[4,5] photocatalytic reactions,[6-8] lithium batteries,[9-12] supercapacitors[13-15] and capacitive deionization[16,17] due to the following outstanding properties. Firstly, the interspace existed in the hierarchical nanostructures is favorable to the diffusion of the ions in solution or the molecular in gas. Secondly, the close connections of different parts of the hierarchical nanostructures make them favorable for the transfer of the carriers like electrons and holes. Moreover, special crystalline facet might be exposed over those monocrystalline nanostructures and is beneficial to the surface reactions. In this regards, flowerlike nanostructures,[6,18] dendritic nanostructures,[7,19] spherical structures[20] *etc.* have been successfully achieved so far and exhibited excellent performances in various applications. For example, some recent efforts have demonstrated that those hierarchical nanostructures preserved their unique properties and were much closer to real applications when they were assembled on metal supports.[21-23] The controlled fabrication of different hierarchical nanostructured materials on different metal substrates and the development of new applications are therefore of great interest.

Transition-metal vanadate nanostructures have recently been reported as very active materials in various applications including high energy density lithium batteries,[24-26] sensors,[27] catalysis[28-33] *etc.* It has been demonstrated that the performances of those vanadates are significantly related to the morphology besides their intrinsic physical and chemical properties. For example, $CuV_2O_6$ nanowires showed enhanced electrode kinetics and higher discharge capacity compared with the bulk particles due to the shorter diffusion route and larger surface area for lithium intercalation.[25] It also has been reported that the metallic substrates supported $Fe_2V_4O_{13}$ nanoribbons were much more convenient for the post-treatment and recycling process during the photocatalytic reactions compared with the powder counterparts.[34] It is understandable that the diffusion of the reactive mediums is significant in the applications of lithium batteries, sensors and catalysis and might be beneficial from the hierarchical nanostructures. However, the mostly reported morphologies of the transition-metal vanadates are nanorods,[35-37] nanowires,[38] nanotubes,[39,40] nanobelts,[25] nanosheets,[41-43] and etc. The fabrication of hierarchical transition-metal vanadate nanostructures, especially assembled on metal supports, is still a big challenge.

Selective catalytic reduction (SCR) has been proved to be the most effective way to control the emission of $NO_x$ which is one of the major air pollution causing photochemical smog, acid rain and ozone depletion.[44,45] Some recent studies indicated that metal wire meshes might be as an alternative support to achieve fast inter-phase mass transfer rates, good mechanical strength

and dust tolerance, due to their controllable mass transport, good thermal, mechanical properties and etc. [3,21] However, the traditional wash-coating method is hard to make the active components uniformly dispersed and fixed, especially hard to preserve the components with specific morphologies, over the metal supports. Therefore, the development of new methods for the steady and uniform loading of specific active components over the metal supports is still a big challenge.

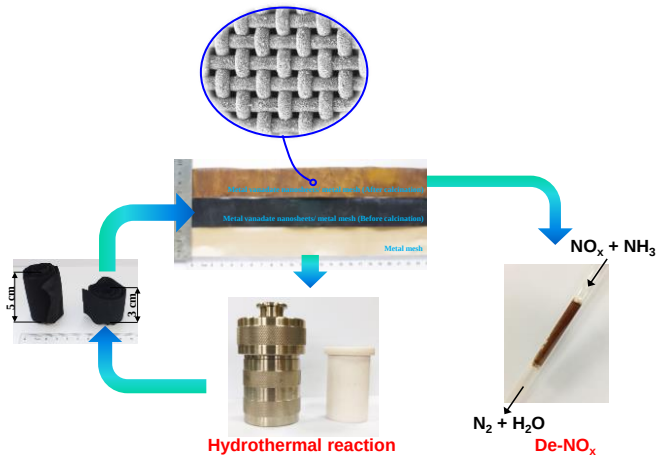


**Fig. 1.** A flow-process diagram of the preparation and application for SCR reaction of the hierarchical transition-metal vanadate nanosheets prepared on metal mesh. The copper meshes with the sizes of 3 cm × 25 cm were firstly *in-situ* grown with the hierarchical vanadate nanostructures through a simple hydrothermal method. The obtained metal meshes were then annealed, forming the hierarchical transition-metal vanadate nanosheets decorated metal supports. For the catalytic application, the samples were rolled up and inserted into a quartz tube for the SCR of $NO_x$.

Herein, we reported a facile and general method to *in-situ* grow hierarchical transition-metal vanadate nanosheets on various metal (Cu, Fe and Ni) supports. As illustrated in Fig. 1, the hierarchical nanostructures decorated on large-scale metal supports could be obtained through a simple hydrothermal reaction and the followed calcination process. The sizes and the thicknesses of the nanosheets could be controlled by adjusting the reaction duration, the acidity of the solution and the concentration of vanadate precursor. It was also demonstrated that the metal supports could be easily scaled up through changing the size of the Teflon-lined stainless steel autoclave. For example, the copper meshes of 3 cm × 25 cm could be scaled up to 5 cm× 25 cm by changing the size of Teflon-lined stainless steel autoclave from 50 ml to 100 ml during the hydrothermal reactions. Base on this property and the flexibility of the metal supports, we used the metal meshes decorated by the hierarchical transition-metal vanadate nanosheets as monolith catalysts for the selective catalytic reduction (SCR) of NO with $NH_3$ for the first time.

## 2. Experimental Section

### 2.1 Synthesis of hierarchical transition-metal vanadate nanosheets

All the reagents were purchased from Sinopharm Chemical Reagent Co. Ltd (China) and were used without further purification. Copper mesh (80 meshes), iron mesh (60 meshes), nickel mesh (60 meshes) and copper foil were purchased from Shanghai Fine Sieving Filtrating Equipment Co., LTD. Copper foam was purchased from Alantum Advanced Technology Materials (Dalian) Co. Ltd. Before use, the metal supports were cut in the desired size and then pretreated with 0.1 M HCl aqueous solution, ethanol and deionized (DI) water successively upon ultrasonic vibration to remove the grease and oxides. The vanadate hierarchical architectures were *in-situ* prepared on the metal supports through a simple hydrothermal method. In a typical process, 1.5 mmol of $NH_4VO_3$ was first dissolved in 40 mL of hot DI water in the polytetrafluoroethylene (PTFE) lining (50 mL). The cleaned metal supports were then immersed into the solution and the lining was transferred to a Teflon-lined stainless steel autoclave for 24 h hydrothermal reaction under 180 °C. After the reaction, the autoclave was cooled down naturally to room temperature. The obtained products were washed with DI water and ethanol for several times. Finally, the products were dried at 80 ℃ for 12 h and calcined in air at 450 °C for 2 h with a ramping rate of 2 °C/min. To adjust the acidic property of the solution, acetic acid (0.1 M) with different amount were added into the $NH_4VO_3$ solution. The total volume of the solution fixed to 40 mL.

### 2.2 Materials characterization

The morphologies were characterized by a scanning electron microscopy (SEM, JEOL, JSM-6700F), a transmission electron microscope (TEM, JEM-200CX) and a field emission high resolution transmission electron microscope (HRTEM, JEM-2100F). Powder X-ray diffraction (XRD) was performed with a Rigaku D/MAX-RB X-ray diffractometer by using Cu Kα (40 kV, 40 mA) radiation and a secondary beam graphite monochromator. Thermogravimetric analysis (TGA, SHIMADZU DTG-60H) was used to investigate the thermal decomposition behavior of the samples. The temperature was increased from room temperature to 900 °C at a rate of 10 °C $min^{-1}$.

### 2.3 Catalytic activity measurements

The SCR activities were test in a fixed-bed quartz micro-reactor (i.d. 7 mm) operating in a steady state flow mode. The typical reactant conditions were as follows: 0.4g catalysts (40-60 mesh), 550 ppm NO, 550 ppm $NH_3$, 3% $O_2$, 10% $H_2O$ (when used) and balance $N_2$. The total flow rate was 500 mL/min leading to a gas hourly space velocity (GHSV) of 26000 $h^{-1}$. The temperature was increased from 100 to 400℃ step by step. At each temperature step the concentrations of NO, $N_2O$ and $NH_3$ were recorded when the SCR reaction reached steady state after 15 min. The concentrations of NO in the inlet and outlet gases were measured by a KM9106 flue gas analyzer. The concentrations of $N_2O$ and $NH_3$ were measured by a Transmitter IR $N_2O$ analyzer and IQ350 ammonia analyzer. The NO conversion and $N_2$ selectivity were calculated

according to the following equations (1) and (2). In equation (2), both NO and $NO_2$ were included in $NO_x$.

$$NO\ \ Conversion(\%) = \frac{[NO]_{in} - [NO]_{out}}{[NO]_{in}} \times 100\% \quad (1)$$

$$S_{N_2} = \left(1 - \frac{2[N_2O]_{out}}{[NO_x]_{in} + [NH_3]_{in} - [NO_x]_{out} - [NH_3]_{out}}\right) \times 100\% \quad (2)$$

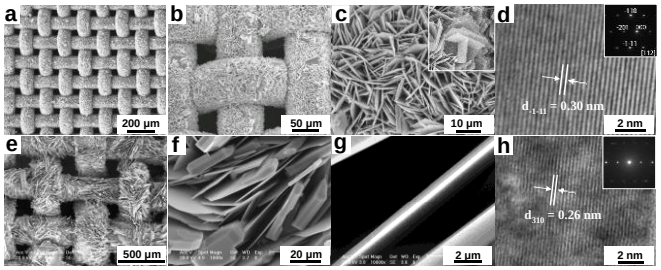


**Fig. 2** FESEM images and HRTEM images of different hierarchical transition-metal vanadate nanosheets prepared on copper mesh (a-d) and iron mesh (e-h). The insets in c, d and h are the amplified FESEM image and SAED patterns, respectively.

## 3. Results and discussion

### 3.1 Fabrication of the hierarchical transition-metal vanadate nanosheets

In the present work, a simple hydrothermal reaction and the followed calcination process were applied to *in-situ* grow vanadate nanostructures over different metal supports. Field-emission scanning electron microscopy (FESEM) images (Fig. 2 a-b, e-f) clearly show that the metal (Cu, and Fe) vanadates are in the form of nanosheets assembled hierarchical nanostructures and uniformly cover on all the metal supports. The copper vanadate nanosheets are in the form of square and closely assembled to flowerlike architectures (Fig. 2c and the inset). The sizes are in the range of several micrometers to dozens of micrometers, while the thickness is about 100 nm-1 μm. The iron vanadate nanosheets are not so uniform and their sizes are larger compared with that of the copper vanadate nanosheets (Fig. 2f, g), but they all grow on the metal skeletons to form a uniform structure (Fig. 2e). We also found that the morphologies of the hierarchical copper vanadate nanostructures can be kept on different shapes of the metal supports under similar preparation conditions. For example, square nanosheets assembled beautiful flowerlike architectures were obtained on copper meshes (Fig. 2 a-c), copper foil (Fig. S1 a-c,) and copper foams (Fig. S1 d-f). On the other hand, the vanadates assembled nanostructures can also be obtained on Ni mesh (Fig. S2). Although their morphologies more like nanobelts rather than like nanosheets. Those results demonstrate that the developed hydrothermal method is versatile for the preparation of hierarchical transition-metal vanadate nanosheets on different transition-metal supports, and all the ordered hierarchical nanostructures are in a highly open structure which is favorable for the diffusion of the reactants in catalytic reactions.

The crystallographic structures of the hierarchical transition-metal vanadate nanosheets were further studied by X-ray diffraction (XRD) and selected-area electron diffraction (SAED). Fig. 3 (a) indicates that almost all the diffraction peaks

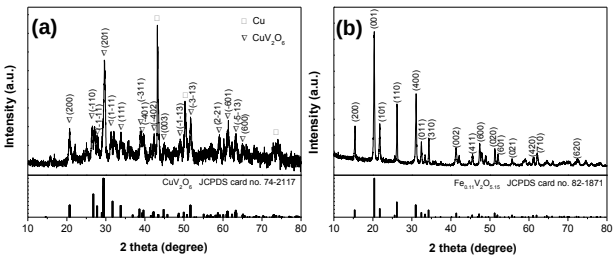


**Fig. 3** XRD patterns of different hierarchical transition-metal vanadate nanosheets prepared on copper mesh (a) and iron mesh (b) after heat treatment.

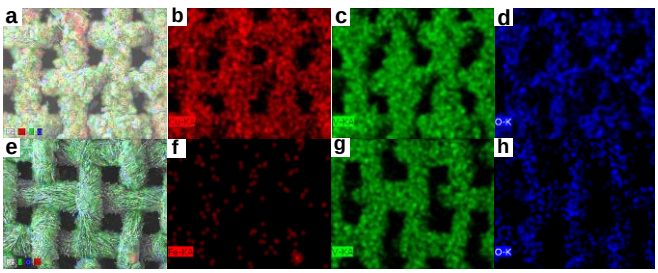


**Fig.4** Elemental mapping images of different hierarchical transition-metal vanadate nanosheets prepared on copper mesh (a-d) and iron mesh (e-h).

can be assigned to triclinic $CuV_2O_6$ (JCPDFS card no. 74-2117), expect for the three typical peaks (2θ of 43.3 °, 50.4 ° and 74.1 °) originated from the copper substrate. For the iron support, all the diffraction peaks can be assigned to orthorhombic $Fe_{0.11}V_2O_{5.15}$ (JCPDFS card no. 82-1871). Interestingly, we also found that the vanadate nanosheets were in the form of monocrystalline as demonstrated by the SAED patterns (the insets in Fig. 2d and h) with the form of diffraction spots. The SAED patterns in Fig. 2d can be indexed to the [112] zone axis of triclinic $CuV_2O_6$. The HRTEM images (Fig. 2 d, h) also show the (-1-11) lattice fringes (0.3 Å) of the $Cu_2VO_6$ nanosheets and the (310) lattice fringes (0.24 Å) of the $Fe_{0.11}V_2O_{5.15}$ nanosheets.

The spatial distributions of the elements were further illustrated by the elemental mapping. Fig. 4 a-d show that the elements of Cu, V and O are well-distributed on the copper support. Fig. 4 e-h show that the elements of V and O are well-distributed on all the iron support, but the iron is not so clear due to the small ratio of Fe element in the orthorhombic $Fe_{0.11}V_2O_{5.15}$. However, this result demonstrates that the $Fe_{0.11}V_2O_{5.15}$ nanosheets covered all the Fe support, otherwise the iron skeleton would be detected. The well-distributed metal elements over the whole metal support would provide even active sites and is significant to the catalytic reactions.

The $N_2$ sorption was performed to detect the surface area and porous structure of $CuV_2O_6$ and $Fe_{0.11}V_2O_{5.15}$. The obtained nitrogen adsorption–desorption isotherms are shown in Fig. S3. It was found that both the catalysts show a type II isotherm, indicative of large amount of macropores in the catalysts. The surface areas and pore volumes of $CuV_2O_6$ and $Fe_{0.11}V_2O_{5.15}$ were 7.01 and 26.7 $m^2/g$, 0.03 and 0.21 $cm^3/g$, respectively. SEM images (Fig. S4d and e) further indicate that pores were obviously observed over annealed $Fe_{0.11}V_2O_{5.15}$ nanosheets but not over annealed $CuV_2O_6$ nanosheets. This result is in accordance with the $N_2$ sorption results. Therefore, the $Fe_{0.11}V_2O_{5.15}$ may have better catalytic performance than $CuV_2O_6$ due to the larger surface area.

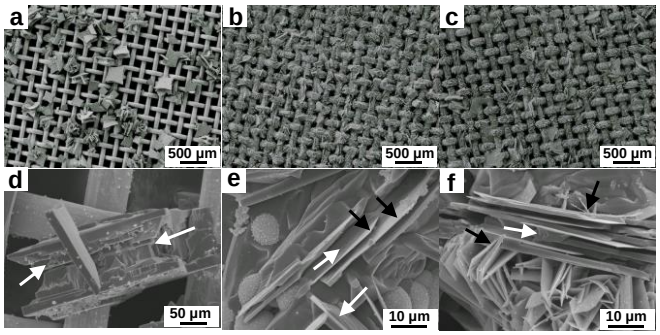


**Fig.5** Morphological evolution of the hierarchical transition-metal vanadate nanosheets prepared on copper mesh at different synthesis stages of 1h (a, d), 2h (b, e) and 3h (c, f).

### 3.2 Formation mechanism of the hierarchical transition-metal vanadate nanosheets

Up to now, since the hierarchical transition-metal vanadate nanosheets over metal supports have rarely been reported, the formation mechanism would be of great interesting. Here we chose copper vanadate on copper mesh as the model to study the formation mechanism. Firstly, the thermal analysis (Fig. S3a) indicates that the copper vanadates have two obvious steps of weight loss ranging from 100 to 200 ℃ and 200 to 320 ℃, which correspond to two steps of water molecule loss, namely the loss of absorbed water and lattice water, respectively.[46,47] This is a typical behavior for the vanadates hydrates. Above 400 ℃, there is a slight increase of the weight which is probably due to the oxidation of copper scraped off from the metal supports. Similar behavior was also observed over the iron mesh (Fig. S4a). It is also found out that the surface of the vanadate nanosheets over copper support become rough after annealing (Fig. S4b-d). It is therefore concluded that the crystalized copper vanadates were obtained through the formation of hydrates during the hydrothermal reaction and the followed dehydration and crystalization process during the heat treatment process.

The evolution of morphologies with different hydrothermal durations was further studied by FESEM. Fig. 5a-c indicates that the sizes of the nanosheets constantly decrease with the increase of hydrothermal duration from 1h to 3h. The detailed changes of the nanosheets are carefully indicated by the high magnification SEM images (Fig. 5d-f). Fig. 5d indicates that the size of the first formed nanosheets at 1 h achieves hundreds of micrometer. Interestingly, the side faces of the nanosheets are obviously etched as indicated by the white arrows. With hydrothermal reaction going on, the side faces are continuously etched (white arrows in Fig. 5e), leading to the formation of thin nanosheets (black arrow in Fig. 5e). After 3 hours of reaction, the etching process is not over yet (white arrow in Fig. 5f), but most of the formed nanosheets are assembled to uniformly arranged hierarchical structures. Here, the nanosheets are in the form of interlaced structure which is probably due to the new nucleation and growth process as indicated by the black arrow in Fig. 5f. Therefore, it is deduced that the orientational etching and new nucleation lead to the formation of hierarchical nanostructure. Remarkably, a similar etching process was also observed in the formation of iron vanadate nanosheets (Fig. S5 a,b).

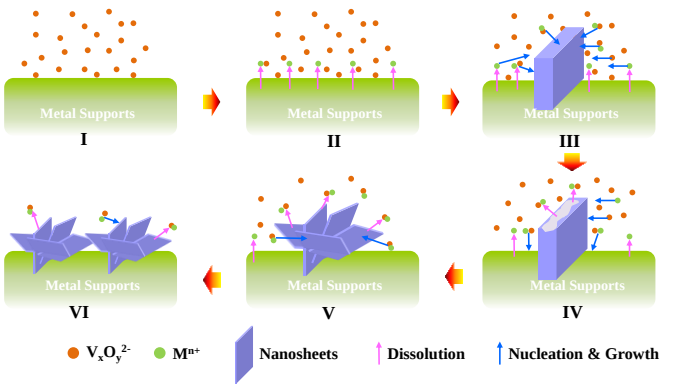


**Fig.6** Schematic illustration of the formation processes occurring at different stages which lead to the of hierarchical transition-metal vanadate nanosheets.

Combined with the above results and discussion, the formation process of the hierarchical transition-metal vanadate nanosheets was proposed in Fig. 6. Before hydrothermal reaction, the vanadium source is in the form of $VO_3^-$ and the transition-metals are in the form of metal supports (Fig. 6 I). With hydrothermal reaction started, the metal starts to dissolve into the solution as ions which are quite easy to nucleate with the vanadates under the hydrothermal conditions (Fig. 6 II). During this period, the dissolution of the metal support is very quick due to that the metal surface is exposed and directly contacted with the solution. Meanwhile, the concentration of vanadates is also high enough to lead to the fast nucleation and growth of metal vanadates. Big vanadate sheets in the micrometer range are formed during this period (Fig. 6 III). However, the big vanadate sheets are not stable. The side surfaces are easy to be orientationally etched probably due to the high surface energy (Fig. 6 IV). With reaction going on, the constant etching process leads to the formation of thin nanosheets. Meanwhile, the dissolved ions again nucleate and grow on the formed nanosheets or the metal supports to form new nanosheets (Fig. 6 V). Finally, nanosheets assembled hierarchical structures are formed and covered all the metal skeletons (Fig. 6 VI). Although the vanadate nanosheets still

suffer the circulation of dissolution and new nucleation and growth, the rate is much lower due to the exhaustion of vanadate precursor and the slow dissolution of the metal supports which are covered by vanadate nanosheets.

According to the above proposed mechanism, the rates of dissolution, nucleation and growth are the main processes that involved in the formation of nanosheets. It is feasible to adjust the morphologies (e.g. size and thickness) of the nanosheets simply through changing the relative rates of dissolution and nucleation. If the rate of dissolution is higher than the rate of nucleation, the formed nanosheets should be much smaller and thinner. For example, if we further increase the hydrothermal duration to 72 h (Fig. S6 a-c), the size and thickness obviously decreased due to the decrease of dissolution rate as described above. On the other hand, the nanosheets with smaller sizes can also be obtained by either increasing the amount of acid to increase the rate of dissolution or decreasing the concentration of vanadate precursor to decrease the rate of nucleation. Corresponding results (Fig. S7 a-f and Fig. S8 a,b) show that the size and thickness of the nanosheets also decreased. On the opposite, the size and thickness of the nanosheets can also increase with the increase of nucleation rate through increasing the concentration of vanadate precursor as illustrated in Fig. S8 c and d.

### 3.3 De-$NO_x$ performance of hierarchical transition-metal vanadate nanosheets

Above results have demonstrated that the hierarchical transition-metal vanadate nanosheets with different sizes on different metal supports can be controllably prepared through the simple hydrothermal-calcination method. In fact, the uniform structures can be prepared in large scale and are scalable as illustrated in Fig. 1. For example, the copper meshes of 3 cm × 25 cm could be scaled up to 5 cm× 25 cm by changing the size of Teflon-lined stainless steel autoclave from 50 ml to 100 ml during the hydrothermal reactions. The vanadate nanosheets assembled hierarchical nanostructures were grown very uniform on the whole metal meshes.

Since the metal supports are easily to be curled or to be cut into different shapes, they can be directly used as devices in practical applications. $FeVO_4$ has recently been reported to hold the promising as $NH_3$-SCR catalyst for $NO_x$ removal both in stationary sources and diesel engines due to its high activity and stability.[32] It also has been reported that the metal meshes or foams are excellent supports for SCR monolith catalysts due to their controllable mass transport, good thermal and mechanical properties.[3,21] In this work, we curled the iron meshes which are decorated by hierarchical transition-metal vanadate nanosheets to form monolith catalysts to explore their application in SCR reactions of $NO_x$ removal. Notably, the thickness of the obtained catalyst is related to the hydrothermal reactions, we only used the hierarchical nanostructure assembled by single layer of vanadate nanosheets for the following catalytic application.

Fig. 7a shows that the temperature window (the temperature range at which the conversion of NO is higher than 80%) for the iron mesh based monolith catalyst ranges from 260 to 360 ℃. The selectivity towards $N_2$ was measured with the increase of reaction temperature. Fig.7a indicates the $N_2$ selectivity was stable and above 98% below 325 ℃, indicating that the catalyst worked quite well during this temperature range. However, the $N_2$ selectivity decreased quickly when the reaction temperature increased to above 325 ℃. This might also be the reason that causes the decrease of NO conversion above 325 ℃. It has been well demonstrated that the true active sites for $FeVO_4$ was the surface enriched $VO_x$ species.[48] We also estimated the specific turnover frequency (TOF) of the

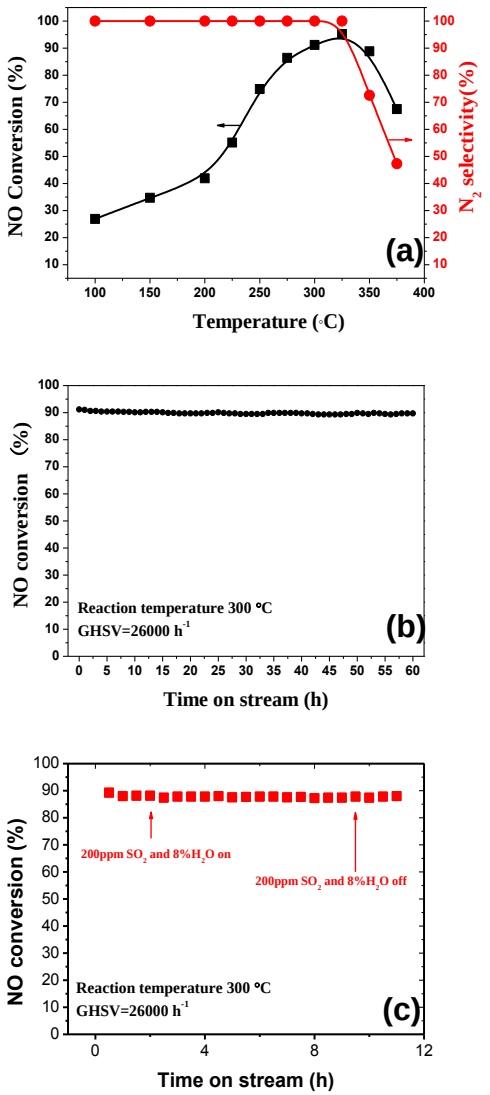


**Fig. 7** The performance of hierarchical iron vanadate nanosheets prepared on iron mesh in the application of SCR of NO with $NH_3$. (a) NO conversion and $N_2$ selectivity as a function of temperature, (b) stability test at 300 °C for 60 h and (c) $SO_2/H_2O$ durability test. The experiments were performed in the feed gas of 500 mL/min total rate, 500ppm NO, 500ppm $NH_3$, 5%$O_2$, and $N_2$ balance, GHSV=26000$h^{-1}$. 200ppm $SO_2$ and 8% $H_2O$ were introduced for the $SO_2/H_2O$ durability test.

hierarchical iron vanadate nanosheets at different temperatures as shown in Table S1. It was found out that the TOFs range from 16.56-29.52 $h^{-1}$ during 150-225 ℃. The reported specific TOFs of vanadia-titania xerogels range from 0.9-18 $h^{-1}$ during 150-227 ℃.[49] It seems that the hierarchical iron vanadate nanosheets showed better activity compared with the most reported vanadia-titania SCR catalyst, which is probably attributed to the specific morphologies and the fast inter-phase mass transfer rates. Fig. 7b shows that the conversion of NO over the iron mesh based monolith catalyst was kept about 90% in 60 h, indicating that the catalyst was quite stable. Besides, since certain amounts of $SO_2$ (30–2000 ppm) and $H_2O$ (2–15 vol%) usually exist in the exhaust and may poison the catalyst due to the adsorption of $SO_2$ and water on the catalyst surface, the effect of $H_2O$ and $SO_2$ on NO conversion over the monolith catalyst was further studied in a feed stream containing 200 ppm $SO_2$ and 8 vol% $H_2O$. Fig. 7c shows that the $NO_x$ conversion almost didn't change with the simultaneous addition and removal of $SO_2$ and $H_2O$. This result demonstrates that the iron mesh based monolith catalyst is highly resistant and reversible to both $SO_2$ and $H_2O$. Therefore, the iron vanadate assembled iron mesh is a promising candidate of de-$NO_x$ monolith catalysts for stationary source at medium temperatures.

## 4. Conclusions

A facile method is developed for large-scale growth of hierarchical transition-metal (Cu, Fe, and Ni) vanadate nanosheets on corresponding metal meshes as supports via a hydrothermal method and afterward calcination process. Those nanosheets are in the form of monocrystalline and are formed through an orientational etching process and simultaneous nucleation and growth process. The morphologies of the hierarchical nanostructures could be controlled by adjusting the balance between dissolution and nucleation rates, such as changing the reaction duration, the acidity and the concentration of vanadate precursor. The size of the metal supports could be easily scaled up by changing the size of Teflon-lined stainless steel autoclave. The iron vanadate nanosheets assembled hierarchical architectures on iron meshes are found effective, highly resistant and reversible to both $SO_2$ and $H_2O$ when they are used as monolith catalysts for SCR of $NO_x$. Therefore, the iron vanadate assembled iron mesh is a promising candidate of de-$NO_x$ monolith catalysts for stationary source at medium temperatures. Besides, we believe the new developed metal supports loaded vanadate nanostructures might be useful in other applications like photocatalysis and lithium batteries.

## Acknowledgements

This work was financially supported by National Natural Science Foundation of China (21303099, U1462110), National Basic Research Program of China (973 Program, 2014CB660803), Shanghai Municipal Education Commission (14ZZ097), Shanghai Municipal Science and Technology Commission(13DZ2292100), Baoshan District Science and Technology Commission of Shanghai (bkw2013142), Research Fund for the Innovation Program of Shanghai University (K.10040713003) and Shanghai Municipal Education Commission (B.37040713001).

## Notes and references

[a] Research Center of Nano Science and Technology, Shanghai University, 99 Shangda Road, Shanghai 200444, China. E-mail: dszhang@shu.edu.cn Fax: +86-21-66136079; Tel: +86-21-66136081.

[b] School of Chemical and Biomedical Engineering, Nanyang Technological University, 62 Nanyang Drive, Singapore 637459, Singapore.

Electronic Supplementary Information (ESI) available: More FESEM and thermal analysis results. See DOI: 10.1039/b000000x/

1. C. Anand, S. Joseph, G. Lawrence, D. S. Dhawale, M. A. Wahab, J. H. Choy and A. Vinu, *Chemcatchem*, 2013, **5**, 1863-1870.
2. D. Liu, W. W. Lei, S. Qin and Y. Chen, *Sci. Rep.*, 2014, **4**, 4453.
3. S. X. Cai, D. S. Zhang, L. Y. Shi, J. Xu, L. Zhang, L. Huang, H. R. Li and J. P. Zhang, *Nanoscale*, 2014, **6**, 7346-7353.
4. T. Y. Jeon, H. C. Jeon, S. Y. Lee, T. S. Shim, J. D. Kwon, S. G. Park and S. M. Yang, *Adv. Mater.*, 2014, **26**, 1422-1426.
5. J. Li, H. Q. Fan and X. H. Jia, *J. Phys. Chem. C*, 2010, **114**, 14684-14691.
6. Y. Wang, S. K. Li, X. R. Xing, F. Z. Huang, Y. H. Shen, A. J. Xie, X. F. Wang and J. Zhang, *Chem.-Eur. J.*, 2011, **17**, 4802-4808.
7. Z. Q. Sun, J. H. Kim, Y. Zhao, F. Bijarbooneh, V. Malgras, Y. Lee, Y. M. Kang and S. X. Dou, *J. Am. Chem. Soc.*, 2011, **133**, 19314-19317.
8. J. Liu, Z. P. Guo, W. J. Wang, Q. S. Huang, K. X. Zhu and X. L. Chen, *Nanoscale*, 2011, **3**, 1470-1473.
9. Y. J. Gong, S. B. Yang, L. Zhan, L. L. Ma, R. Vajtai and P. M. Ajayan, *Adv. Funct. Mater.*, 2014, **24**, 125-130.
10. J. M. Haag, G. Pattanaik and M. F. Durstock, *Adv. Mater.*, 2013, **25**, 3238-3243.
11. G. X. Wang, B. Wang, X. L. Wang, J. Park, S. X. Dou, H. Ahn and K. Kim, *J. Mater. Chem.*, 2009, **19**, 8378-8384.
12. L. Li, K. H. Seng, Z. X. Chen, Z. P. Guo and H. K. Liu, *Nanoscale*, 2013, **5**, 1922-1928.
13. Z. Li, L. Zhang, B. S. Amirkhiz, X. H. Tan, Z. W. Xu, H. L. Wang, B. C. Olsen, C. M. B. Holt and D. Mitlin, *Adv. Energy Mater.*, 2012, **2**, 431-437.
14. L. L. Jiang and Z. J. Fan, *Nanoscale*, 2014, **6**, 1922-1945.
15. J. Y. Tao, N. S. Liu, L. Y. Li and Y. H. Gao, *Nanoscale*, 2014, **6**, 2922-2928.
16. H. Wang, L. Y. Shi, T. T. Yan, J. P. Zhang, Q. D. Zhong and D. S. Zhang, *J Mater Chem A*, 2014, 2, 4739 - 4750.
17. X. Wen, D. Zhang, T. Yan, J. Zhang and L. Shi, *J. Mater. Chem. A*, 2013, **1**, 12334-12344.
18. J. G. Hou, C. Yang, H. J. Cheng, Z. Wang, S. Q. Jiao and H. M. Zhu, *Phys. Chem. Chem. Phys.*, 2013, **15**, 15660-15668.
19. M. Pan, S. X. Xing, T. Sun, W. W. Zhou, M. Sindoro, H. H. Teo, Q. Y. Yan and H. Y. Chen, *Chem. Commun.*, 2010, **46**, 7112-7114.
20. H. Wu, F. Bai, Z. C. Sun, R. E. Haddad, D. M. Boye, Z. W. Wang, J. Y. Huang and H. Y. Fan, *J. Am. Chem. Soc.*, 2010, **132**, 12826-12828.



 

21. H. Li, D. Zhang, P. Maitarad, L. Shi, R. Gao, J. Zhang and W. Cao, *Chem. Commun.*, 2012, **48**, 10645-10647.
22. C. Z. Yuan, J. Y. Li, L. R. Hou, X. G. Zhang, L. F. Shen and X. W. Lou, *Adv. Funct. Mater.*, 2012, **22**, 4592-4597.
23. C. Z. Yuan, L. Yang, L. R. Hou, L. F. Shen, X. G. Zhang and X. W. Lou, *Energy Environ. Sci.*, 2012, **5**, 7883-7887.
24. S. J. Lei, K. B. Tang, Y. Jin and C. H. Chen, *Nanotechnology*, 2007, **18**, 175605.
25. J. G. Yu, J. C. Yu, W. K. Ho, L. Wu and X. C. Wang, *J. Am. Chem. Soc.*, 2004, **126**, 3422-3423.
26. L. Zhou, W. J. Cui, J. M. Wu, Q. F. Zhao, H. X. Li, Y. Y. Xia, Y. H. Wang and C. Z. Yu, *Nanoscale*, 2011, **3**, 999-1003.
27. S. S. Liu, F. Hu, J. Zhang, H. X. Tang and M. W. Shao, *ACS Appl. Mater. Interfaces*, 2013, **5**, 3208-3211.
28. K. Routray, W. Zhou, C. J. Kiely and I. E. Wachs, *ACS Catal.*, 2011, **1**, 54-66.
29. V. Soenen, J. M. Herrmann and J. C. Volta, *J. Catal.*, 1996, **159**, 410-417.
30. D. E. Wang, R. G. Li, J. Zhu, J. Y. Shi, J. F. Han, X. Zong and C. Li, *J. Phys. Chem. C*, 2012, **116**, 5082-5089.
31. R. G. Li, F. X. Zhang, D. G. Wang, J. X. Yang, M. R. Li, J. Zhu, X. Zhou, H. X. Han and C. Li, *Nat. Commun.*, 2013, **4**, 1432.
32. L. Huang, L. Y. Shi, X. Zhao, J. Xu, H. R. Li, J. P. Zhang and D. S. Zhang, *Crystengcomm*, 2014, **16**, 5128-5133.
33. Y. X. Liu, H. X. Dai, J. G. Deng, L. Zhang and C. T. Au, *Nanoscale*, 2012, **4**, 2317-2325.
34. P. Li, Y. Zhou, W. G. Tu, Q. Liu, S. C. Yan and Z. G. Zou, *Chempluschem*, 2013, **78**, 274-278.
35. J. F. Liu, L. L. Wang, X. M. Sun and X. Q. Zhu, *Angew. Chem.-Int. Edit.*, 2010, **49**, 3492-3495.
36. S. Eda, M. Fujishima and H. Tada, *Appl. Catal. B-Environ.*, 2012, **125**, 288-293.
37. B. Yan, S. P. Wang, H. X. Yang, L. J. Feng, H. Y. Wei and Y. Z. Yang, *Asian J. Chem.*, 2013, **25**, 4315-4318.
38. W. Hu, X. B. Zhang, Y. L. Cheng, C. Y. Wu, F. Cao and L. M. Wang, *ChemSusChem*, 2011, **4**, 1091-1094.
39. H. J. Muhr, F. Krumeich, U. P. Schonholzer, F. Bieri, M. Niederberger, L. J. Gauckler and R. Nesper, *Adv. Mater.*, 2000, **12**, 231-234.
40. Y. Wang and G. Z. Cao, *J. Mater. Chem.*, 2007, **17**, 894-899.
41. Y. Zhao, K. Yao, Q. Cai, Z. J. Shi, M. Q. Sheng, H. Y. Lin and M. W. Shao, *Crystengcomm*, 2014, **16**, 270-276.
42. Y. L. Wang, X. Y. Xu, C. B. Cao, C. Shi, W. Mo and H. S. Zhu, *J. Power Sources*, 2013, **242**, 230-235.
43. H. O. Zhu, X. M. Qin, X. Sun, W. S. Yan, J. L. Yang and Y. Xie, *Sci Rep*, 2013, **3**.
44. I. Malpartida, O. Marie, P. Bazin, M. Daturi and X. Jeandel, *Appl. Catal. B-Environ.*, 2012, **113**, 52-60.
45. H. Hamada and M. Haneda, *Appl. Catal. A-Gen.*, 2012, **421**, 1-13.
46. E. Baudrin, S. Denis, F. Orsini, L. Seguin, M. Touboul and J. M. Tarascon, *J. Mater. Chem.*, 1999, **9**, 101-105.
47. E. Baudrin, S. Laruelle, S. Denis, M. Touboul and J. M. Tarascon, *Solid State Ion.*, 1999, **123**, 139-153.
48. F. Liu, H. He, Z. Lian, W. Shan, L. Xie, K. Asakura, W. Yang, H. Deng, *J. Catal.*, 2013, **307**, 340–351.
49. P.H. Mutin, A. F. Popa, A. Vioux, G. Delaha and B. Coq, *Appl. Catal. B-Environ.*, 2006, **69**, 49–57.